Highly Ordered Nanoassemblies of Janus

Spherocylindrical Nanoparticles Adhering to Lipid

Vesicles

Abash Sharma,[†] Yu Zhu,^{†,‡} Eric J. Spangler,[†] Thang B. Hoang,[†] and Mohamed

Laradii*,†

†Department of Physics and Materials Science, The University of Memphis, Memphis, Tennessee

38152, United States

‡Borch Department of Medicinal Chemistry and Molecular Pharmacology, Purdue University,

West Lafayette, Indiana 47907, United States

E-mail: mlaradji@memphis.edu

Abstract

In recent years, there has been a heightened interest in the self-assembly of nanoparticles

(NPs) that is mediated by their adsorption onto lipid membranes. The interplay between the

adhesive energy of NPs on a lipid membrane and the membrane's curvature energy causes it to

wrap around the NPs. This results in an interesting membrane curvature-mediated interaction,

which can lead to the self-assembly of NPs on lipid membranes. Recent studies have demon-

strated that Janus spherical NPs, which adhere to lipid vesicles, can self-assemble into well-

ordered nanoclusters with various geometries, including a few Platonic solids. The present

study explores the additional effect of geometric anisotropy on the self-assembly of Janus NPs

on lipid vesicles. Specifically, the current study utilized extensive molecular dynamics sim-

ulations to investigate the arrangement of Janus spherocylindrical NPs on lipid vesicles. We

1

found that the additional geometric anisotropy significantly expands the range of NPs' self-assemblies on lipid vesicles. The specific geometries of the resulting nanoclusters depend on several factors, including the number of Janus spherocylindrical NPs adhering to the vesicle and their aspect ratio. The lipid membrane-mediated self-assembly of NPs, demonstrated by this work, provides an alternative cost-effective route for fabricating highly engineered nanoclusters in three dimensions. Such structures, with the current wide range of material choices, have great potential for advanced applications, including biosensing, bioimaging, drug delivery, nanomechanics, and nanophotonics.

Keywords: Self-Assembly, Janus Nanoparticles, Lipid Membranes, Nanoclusters, Nanorods, Molecular Dynamics Simulations

Introduction

Nanostructured materials have tremendous potential in many advanced applications, including high-density data storage, ^{1,2} energy storage, ³ solar energy conversion, ⁴ nanophotonics, ^{5,6} catalysis, ^{7,8} targeted drug delivery, ⁹ biosensing, ^{10–12} and gene transfection. ^{13,14} A lot of progress has been made during recent years in the development of fabrication tools for the manufacture of nanostructured materials. ^{15–17} The fabrication of nanostructured materials typically follows a top-down or a bottom-up approach. The top-down approach uses a sequence of steps that employ techniques such as femtosecond laser nanolithography, ¹⁸ electron beam lithography, ¹⁹ and sputtering. ²⁰ The bottom-up approach, on the other hand, leverages the mechanism of nanoparticles (NPs) self-assembly, which is typically mediated by a soft agent such as copolymers, ²¹ DNA or RNA, ^{22–27} proteins, ^{28,29} cellulose, ³⁰ polysaccharides, ³¹ surfactants, ³² and liquid crystals. ³³ Bottom-up approaches have been used to synthesize various nanoassemblies, including dimers, ³⁴ trimers, ³⁵ tetramers, ³⁶ icosamers, ³⁷ pyramids, ³⁸ tori, ²⁵ and chiral structures. ^{39–41}

Lipid membranes are fascinating quasi-two-dimensional fluid and deformable materials. 42 The adhesion of an NP with uniform surface to a lipid membrane, resulting from attractive forces between the two, leads to the deformation of the membrane such that it conforms to the NP's

surfaces. Competition between the NP-membrane adhesive energy and the membrane's curvature energy dictates the degree of wrapping of the NP^{43–46} by the membrane and induces an effective interaction between the NPs. ^{47–50} This effective membrane-curvature-mediated interaction can be attractive and leads to NPs' self-assembly on the membrane, as has been shown by numerous experimental ^{51–58} and theoretical ^{59–64} studies.

At weak adhesive interactions, the degree of wrapping of NPs by lipid membranes is weak. In this case, the NPs are dispersed on the membrane and are fairly diffusive. ⁶⁴ In contrast, the NPs are either highly wrapped or endoyctosed by membranes at low tension and high adhesive interactions. ^{43,64} At intermediate adhesive interactions, however, the deformations caused by the adhesion of the NPs to the membrane extend over length scales well beyond the size of the NPs and give rise to an effective membrane-curvature-mediated interaction between them. ^{48,49,65} Experiments and simulations have shown that this interaction can result in NPs' aggregation into in-plane or out-of-plane linear chains. ^{50,52,56,60,61,64,66–68} Two generic aspects of these assemblies are that they are linear, and neighboring NPs within the assemblies are practically in contact with each other.

Many emerging applications require nanoassemblies in which the NPs are apart from each other. The limitations of lipid membranes in self-assembling NPs into aggregates with geometries other than linear, and such that the NPs are distant from each other, can be overcome through their surface modification into Janus NPs (JNPs). These JNPs are overall hydrophilic and, therefore, fundamentally different from the more conventional amphiphilic Janus NPs. ^{69,70} Namely, they consist of two apposed moieties, with one moiety that interacts more attractively with the lipid head groups than the solvent, while the other moiety interacts more attractively with the solvent. ^{71–73} This surface modification promotes strong adhesion of one moiety to the membrane while the other remains exposed to the aqueous solution. This results in the suppression of spontaneous endocytosis of the JNPs and the emergence of an effective membrane-curvature-mediated repulsive interaction between the JNPs. ^{72,73}

We showed recently that the adhesion of JNPs to lipid vesicles leads to their self-assembly into

various surprisingly ordered nanoclusters, including three Platonic solids, where the JNPs are distant from each other. ⁷⁴ We also showed, in a more recent study, that the adhesion of spherical JNPs onto planar membranes can lead to their self-assembly into ordered non-closed packed hexagonal superlattices, with a lattice constant determined by their number density on the membrane. ⁷⁵ These investigations were performed in the context of spherical Janus NPs. Thanks to recent advances in nanomaterial synthesis, anisotropic nanoparticles with varying geometries, dimensions, and surface properties can be engineered. ⁷⁶ Geometric anisotropy of NPs allows for more tunability of their properties. 77 Earlier studies of membrane-mediated interaction between nanorods or spherocylindrical NPs considered only the case where the NPs' surfaces are chemically uniform. 50,68,78,79 Here as well, membrane curvature induces an effective attractive interaction between the NPs. In this case, the elongated NPs are either dispersed or form tip-to-tip aggregates. 50,68 The following question then arises: How would an additional shape anisotropy to Janus NPs affect their nanoassembly on lipid vesicles? To answer this question, we conducted a sizeable systematic set of molecular dynamics simulations of a coarse-grained implicit-solvent model of several adhering Janus spherocylindrical NPs (JSCNPs) to lipid vesicles. More specifically, we investigated the effects of the aspect ratio and number of adhering JSCNPs on their arrangement on the vesicle. The results demonstrate that geometric anisotropy of the Janus NPs increases significantly the diversity of their highly ordered nanoassemblies.

Results and Discussion

Adhesion of Two JSCNPs to a Vesicle

We first performed a series of simulations of two JSCNPs adhering to a lipid vesicle in order to determine their preferred placement on the vesicle at equilibrium. In these simulations, a pair of parallel JSCNPs, which are very close to each other, are initially placed in close proximity to an equilibrated vesicle. Fig. 1(A), which depicts the time dependence of the distance between the centers of two JSCNPs, with aspect ratio $\alpha = 1.6$ and 4, demonstrates that right after their adhesion,

the two JSCNPs drift away from each other toward an equilibrium state in which they are apart, regardless of their aspect ratio. Furthermore, Fig. 1(A) shows that the relative equilibrium positions of the JSCNPs do not exhibit a lot of fluctuations. However, Fig. 1(B) shows that the amplitude of orientational fluctuations decreases with α but remains overall small, indicating that the two JSCNPs prefer to be mostly parallel.

To confirm that the non-dimerized state of two JSCNPs on a vesicle is preferred, we performed free energy calculations using the weighted histogram analysis method, ⁸⁰ in conjunction with a large number of umbrella sampling simulations. ⁸¹ Here, the reaction coordinate corresponds to the distance between the JSCNPs' center (c) beads. The obtained free energy versus the distance between the JSCNPs' centers, shown in Fig. 1(C) for the case of $\alpha = 1.6$, demonstrates that the absolute minimum of the free energy corresponds to the state where the JSCNPs are distant, namely, the monomeric state. The value of the distance between the JSCNPs, corresponding to the absolute minimum ($\approx 37 \, \text{nm}$), agrees with the equilibrium value of the distance obtained from the unbiased molecular dynamics simulation shown in Fig. 1(A).

Fig. 1(C) shows the existence of a metastable dimeric state in which the JSCNPs lie parallel to each other with a distance between their centers slightly higher than the JSCNPs' diameter D_N . However, this state never emerges in the unbiased simulations, even when the JSCNPs were initially placed such that they are very close to each other, as demonstrated by the far left snapshot in Fig. 1(A). The reason why the JSCNPs do not dimerize is as follows. Right after their adhesion, the JSCNPs are only weakly wrapped by the membrane and are, as a result, fairly mobile. Furthermore, the conformation of the vesicle following the initial adhesion of the JSCNPs remains almost spherical and, therefore, substantially different from the well-deformed conformation of the vesicle when the JSCNPs are in the dimeric state (far left snapshot in Fig. 1(B) versus far left snapshot in Fig. 1(C)). Moreover, since the energy penalty from the monomeric to the dimeric state is much higher than $k_B T$, as demonstrated by Fig. 1(C), the JSCNPs cannot spontaneously revert to the dimeric state once they are far apart. It is interesting that in the dimeric mode, the two JSCNPs are arranged side-by-side, whereas spherocylindrical NPs with uniform surfaces form

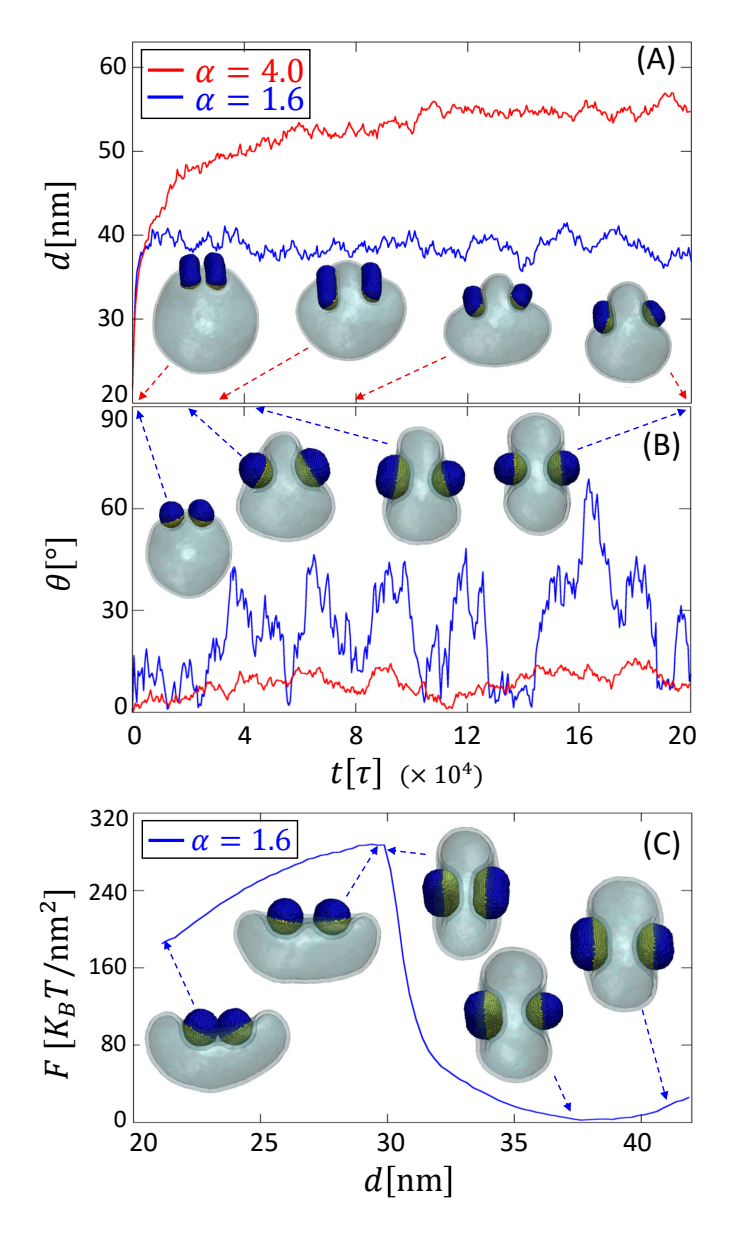


Figure 1: (A) Distance between the centers of two JSCNPs versus time for two aspect ratio values. The two JSCNPs are initially placed adjacent to each other and very close to an equilibrated vesicle. (B) The angle between the two JSCNPs in (A) versus time. (C) Free energy of a vesicle with two JSCNPs as a function of distance between their centers in the case of $\alpha = 1.6$. Snapshots in (A) and (B) show the time evolution of the configuration of the system. Snapshots in (C) are obtained from the WHAM simulations. In these snapshots, the membrane is icy blue, and the moiety of the JSCNPs that interacts attractively (repulsively) with the lipid membrane is yellow (blue). The simulations are performed at an adhesion energy density $\xi = 4.11 \, \text{nm}^2/k_BT$ and area fraction of a JSCNP that adheres to the membrane J = 0.4.

tip-tip aggregates, as was shown earlier by Petrova et al. 68 and Sharma et al. 50

The simulations above were performed on a vesicle of diameter $D_V = 73$ nm. The relative deformation of the vesicle is expected to be reduced as its diameter is increased. To test whether the dimeric state may occur for larger vesicles, we performed a simulation with the same initial conditions and value of the adhesion energy density, ξ , as above, but on a vesicle with $D_V = 120$ nm and found that the JSCNPs do not dimerize in this case as well (see Fig. S3 in the Supporting Information). This indicates that the dimeric state is likely not preferred, regardless of the size of the vesicle, although simulations on vesicles that are much larger than the JSCNPS are necessary to infer the stability of the monomeric state in the case of large vesicles. Overall, the preferred placement of two JSCNPs on a vesicle is therefore similar to that of Janus spherical NPs on a vesicle. ^{72,73} We note that the results above were obtained in the case where the fraction of a JSCNP's area that adheres to the membrane is J = 0.4. Further simulations are also needed to infer the effect of J on the mode of adhesion of two JSCNPs on a lipid vesicle. At higher values of J, it is possible that the dimeric state of two JSCNPs becomes more stable than the monomeric state, as was observed earlier in the case of Janus spherical NPs. ⁷³

Now that we have established that adhering JSCNPs to lipid vesicles experience an effective repulsive interaction, the remainder of this article is focused on determining and characterizing the preferred arrangements of more than two JSCNPs on lipid vesicles. These arrangements are characterized by (1) the radial distribution function (RDF) of the JSCNPs' center beads, which is defined as the normalized distribution of the distance between the NPs' centers of mass, (2) the bond angle distribution (BAD), which is defined as the distribution of the bond angle of a triplet of NPs as defined from their centers of mass, (3) the angles between the axes of the JSCNPs, and (4) their nematic order, whose calculation is described in Section S5 in the Supporting Information. ⁸² In the calculation of the BAD, we only use triplets in which all JSCNPs' center beads are nearest neighbors.

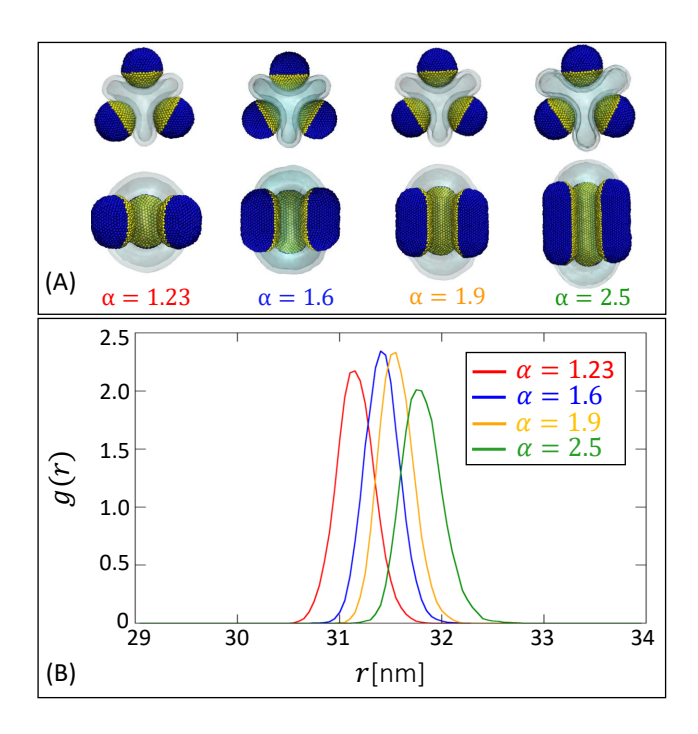


Figure 2: (A) Two different views of snapshots of the vesicle with three JSCNPs for three different aspect ratio values. (B) Radial distribution function, g(r), of the JSCNPs center beads, for different values of α . In these simulations, $\rho = A_V/3A_N = 1.2$, where A_V and A_N are the net areas of the vesicle and a single JSCNP, respectively. Values of ξ and J are the same as in Fig. 1.

Adhesion of Three JSCNPs to a Vesicle

Fig. 2(A) shows that three JSCNPs form a highly ordered nanocluster, in which their centers form an equilateral triangle, similar to the case of spherical Janus NPs. ⁷⁴ This is confirmed by the corresponding RDFs in Fig. 2(B), which exhibit a single peak regardless of the value of α . Fig. 2(A) also shows that the three JSCNPs are arranged such that they are perpendicular to the plane containing their center beads. The general features of nanoclusters composed of three JSCNPs are, therefore, independent of their aspect ratio. These include, in particular, the fact that the angles between the JSCNPs' axes are close to zero (Fig. 1(A) and (B)), independent of the aspect ratio, leading to a nematic order parameter close to 1 (Fig. S4).

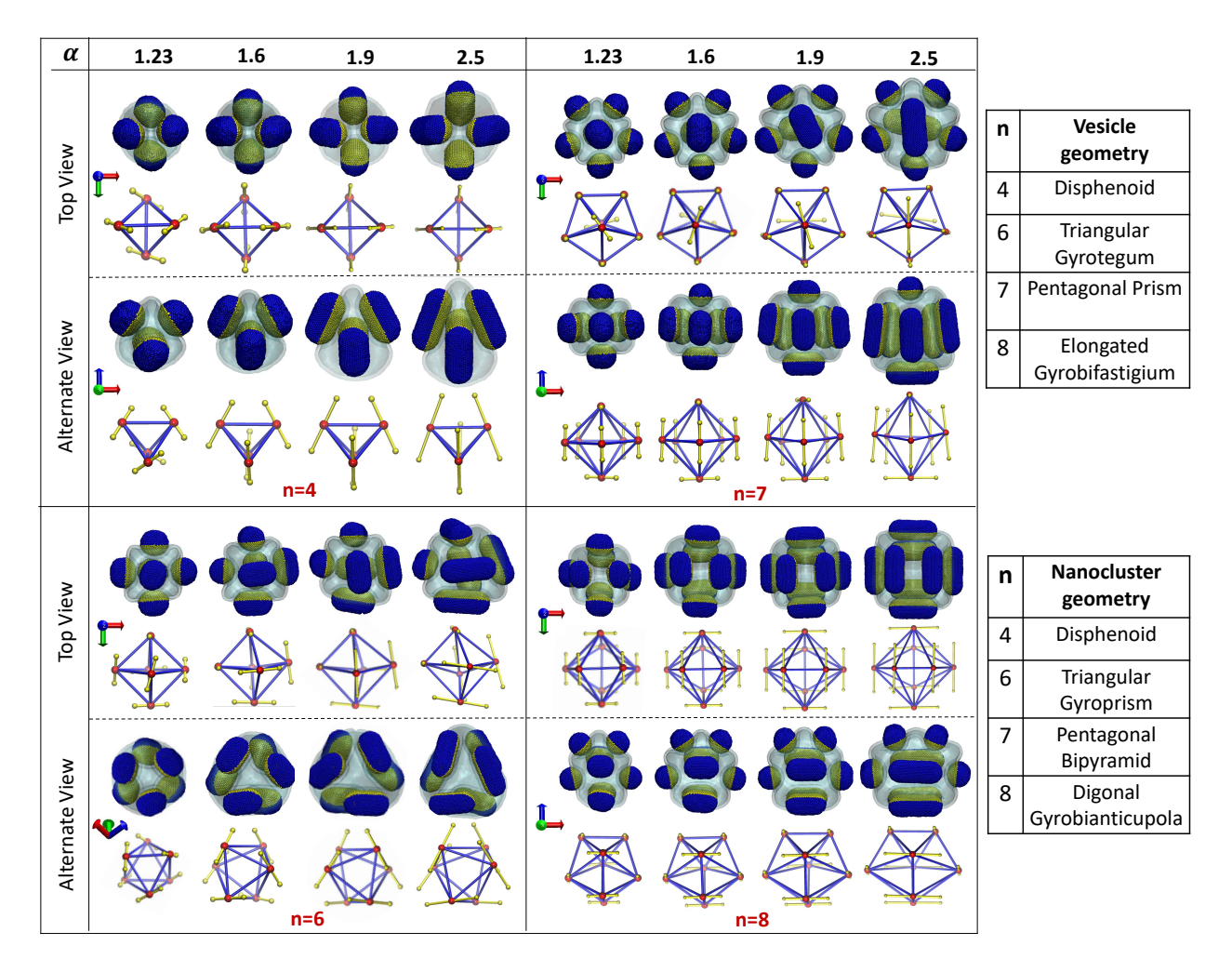


Figure 3: Snapshots of the vesicle with the JSCNPs at values of n ranging between 4 and 8 and for different aspect ratio values. The first and third rows for each value of n show two views of the vesicle with the JSCNPs. The second and fourth rows for each value of n show different views of the geometries of the JSCNPs' nanoclusters obtained from time averages of their positions at equilibrium. Red spheres correspond to the center beads of the JSCNPs. Yellow segments represent the axes of the JSCNPs. Blue segments correspond to links between nearest neighbor JSCNPs obtained from the Delaunay triangulation. Names of the geometries of the vesicles and corresponding nanoclusters for different values of n are shown on the top and bottom tables, respectively. Here, values of ξ and J are same as in Fig. 1.

Adhesion of more than Three JSCNPs to a Vesicle

Configuration snapshots, at equilibrium, of n JSCNPs adhering to a vesicle, in the cases of n=4, 6, 7, and 8 at $\alpha=1.23$, 1.6, 1.9 and 2.5, are shown in Fig. 3. Here, the first and third rows, for each value of n, depict different views of the system. The second and fourth rows show corresponding polyhedra whose vertices (red points) are time-averaged positions of the JSCNPs' center beads at equilibrium. The edges (blue segments), which are links between nearest neighbor JSCNPs, are obtained using spherical Delaunay triangulation based on the JSCNPs' center beads. ⁸³ The yellow segments correspond to the time-averaged directions of the JSCNPs. Fig. 3 demonstrates that JSCNPs' adhesion to lipid vesicles leads them to form strikingly ordered nanoassemblies with details that depend strongly on the value of n. In particular, the JSCNPs' centers form mostly highly symmetric, strictly convex polyhedra. The JSCNPs' orientations in these nanoclusters tend to be highly correlated and depend on the locations of the respective JSCNPs on the polyhedra. Although we have not performed a systematic set of simulations for the case of n=5, a simulation of five JSCNPs at the aspect ratio $\alpha=1.9$ demonstrates a highly ordered nanocluster here as well, as shown by Fig. S4 in the Supporting Information.

Snapshots in the second and fourth rows of Fig. 3, corresponding to n = 4 at $\alpha = 1.23$, demonstrate that the centers of the JSCNPs form a tetrahedron, similar to that of 4 Janus spherical NPs on a lipid vesicle.⁷⁴ The almost regular nature of this structure is demonstrated by the fact that its corresponding RDF, shown by the red curve in Fig. 4(A) for n = 4, exhibits a single peak.⁷⁴ The corresponding BAD (red curve in Fig. 4(C) for n = 4) exhibits two peaks that are close to 60°, in contrast to the single well-defined peak at 60° in the case of 4 spherical Janus NPs.⁷⁴ This implies that the center beads' polyhedron is slightly distorted from the regular polyhedron. Although 4 JSCNPs' centers are localized in space, relative to each other, the orientations of their axes exhibit a high amount of fluctuations at low values of α , as demonstrated by the time dependence of the angles between their axes shown in Fig. 5(A).

Fig. 4(A) shows that the single peak of the RDF, in the case of n = 4 at $\alpha = 1.23$, bifurcates into two distinct peaks as the aspect ratio increases. The corresponding BADs, shown in Fig. 4(C),

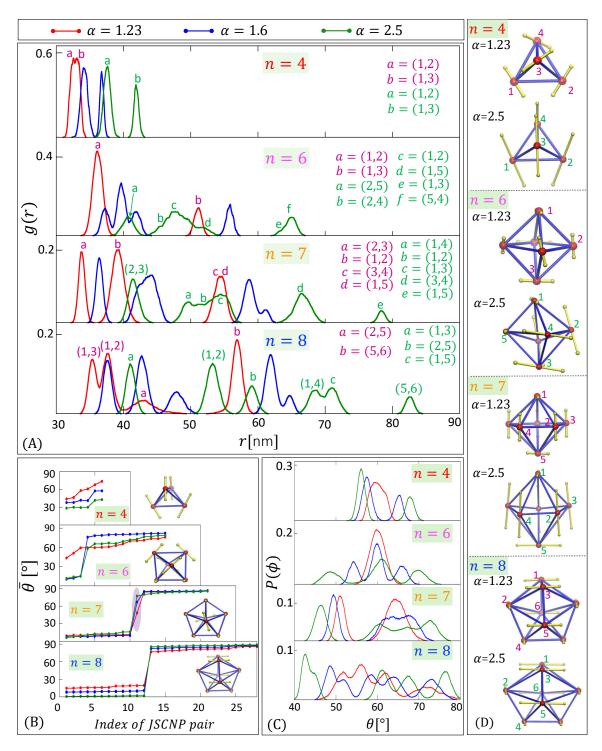


Figure 4: (A) Radial distribution functions (RDFs) of the JSCNPs' center beads, g(r), for different values of n. The peaks are due to correlations of JSCNPs' pairs with indices indicated on the right and in (D). (B) Average angle, $\bar{\theta}$, between the directions of two JSCNPs versus the index of the pair for different values of n. Here, the indices are ordered, such as $\bar{\theta}$ is an ascending function of the index. Note that for each value of n, there are n(n-1)/2 values of the pair index. (C) Bond angle distributions (BADs), $P(\phi)$, for different values of n. (D) Geometries of the JSCNPs' nanoclusters. Indices of the JSCNPs are used to describe the peaks of the RDF in (A).

also exhibit two distinct peaks as α is increased. Therefore, the geometry of the polyhedron, corresponding to 4 JSCNPs, which is close to a regular tetrahedron at low values of α , evolves into an elongated tetrahedron, i.e., a disphenoid, as α is increased. These disphenoid nanoclusters comprise four congruent acute isosceles triangles whose vertex angle decreases with increasing α . Furthermore, Fig. 4(B), which depicts average values of the angles between the axes of any two JSCNPs in the nanocluster, shows that in the case of n=4, all angles decrease with increasing α . This results in the increase of the namatic order parameter S with α , S shown in Fig. S4. Furthermore, Figs. 5(A) and (B) show that the amount of fluctuations in the angles between the JSCNPs' axes decreases drastically with increasing α in the case of n=4. Hence, while the JSCNPs' centers form a well-ordered disphenoid nanocluster for the considered values of the aspect ratio, the relative orientations of the JSCNPs are fluid at low α but become increasingly rigid with increasing α .

Based on the above, the following question arises: Why is the arrangement of 4 JSCNPs not equivalent to that of 3 JSCNPs shown in Fig. 2? In other words, why are the 4 JSCNPs not parallel to each other, with their center beads arranged in a square or a rectangle? To answer this question, we performed a biased simulation that favors an arrangement of the 4 JSCNPs such that they are parallel to each other and their centers form a rectangle. This biased simulation is based on additional three-body interactions, with details found in Section S6 in the Supporting Information. These correspond to a set of three-body potential energies between the center beads, which bias the JSCNPs to adopt a rectangular geometry, and a set of three-body potential energies between the JSCNPs' poles, which bias them to be parallel.

The biased simulations resulted in a long-lived intermediate state in which the JSCNPs' center beads form a square configuration and are parallel, as shown by snapshot (A) in Fig. S8 in the Supplementary Information. Interestingly, the square state then spontaneously evolves into a rectangular state, shown by snapshots (B) in Fig. S8 in the Supplementary Information. This implies that the biased rectangular state is more stable than the square state. Once the biased interaction is turned off, the rectangular configuration rapidly transforms into the same disphenoid structure

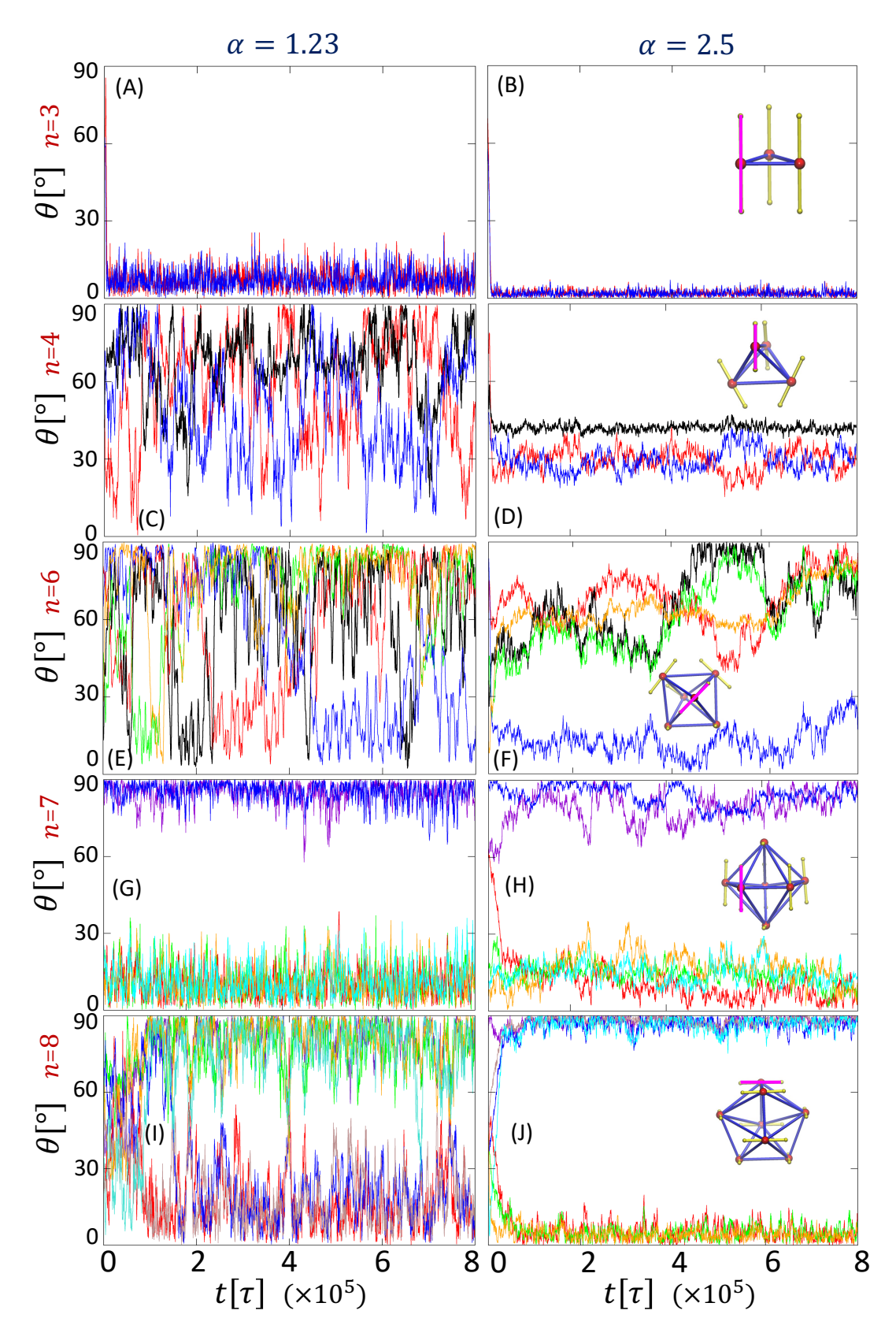


Figure 5: Angles between the JSCNPs' axes versus time for different values of n and α . The angles shown are between the JSCNP, indicated by the pink segment in the snapshots, and the other (n-1) JSCNPs, indicated by yellow segments.

obtained from the unbiased simulation (see snapshots (C) and (D) in Fig. S8 in the Supplementary Information). Therefore, the disphenoid nanocluster must be more stable than the square or rectangular nanocluster. To confirm the stability of the disphenoid nanocluster, we calculated the net adhesion energy of the JSCNPs on the membrane and the curvature energy of the vesicle. Fig. S7 in the Supporting Information shows that the adhesion energy is independent of the geometry of the nanocluster. This is not surprising since the JSCNP moieties, which interact favorably with the lipids, are fully wrapped by the membrane, regardless of the JSCNPs' placement on the vesicle. Therefore, the relative stability of the different structures is dictated by the vesicle's curvature energy, which is calculated using an approach based on the Helfrich Hamiltonian⁸⁴ in conjunction with a local Monge representation ⁶⁴ (see details of this approach are found in Section S8 in the Supporting Information). Fig. S8 in the Supplementary Information demonstrates that the curvature energy of the rectangular nanocluster is lower than that of the square nanocluster, which explains the spontaneous transformation of the square nanocluster into a rectangular nanocluster. More importantly, Fig. S8 in the Supplementary Information shows that the curvature energy of the disphenoid nanocluster is lowest, confirming the stability of the disphenoid nanocluster against the square or rectangular nanoclusters.

We now turn to the case of n=6, whose configurations at different values of α are shown in Fig. 3. At $\alpha=1.23$, the nanocluster formed by the centers of the 6 JSCNPs is almost a regular octahedron, and the geometry of the corresponding vesicle is close to a cube, very similar to the case of 6 Janus spherical NPs.⁷⁴ The regular octahedral structure of the 6-JSCNPs' nanocluster, at $\alpha=1.23$, is demonstrated by its corresponding RDF, shown in Fig. 4(A), which exhibits two peaks with a ratio between their positions that is very close to $\sqrt{2}$. This octahedral structure is also confirmed by its corresponding BAD, shown in Fig. 4(C), which exhibits a single peak at $\phi=60^{\circ}$. Despite the ordered placement of the centers of 6 JSCNPs at $\alpha=1.23$, Fig. 5(C) shows that their relative orientations exhibit a high degree of fluctuations, similar to the case of 4 JSCNPs. Interestingly, however, Fig. 5(C) shows that these fluctuations are localized around either low or large values, with frequent transitions between them.

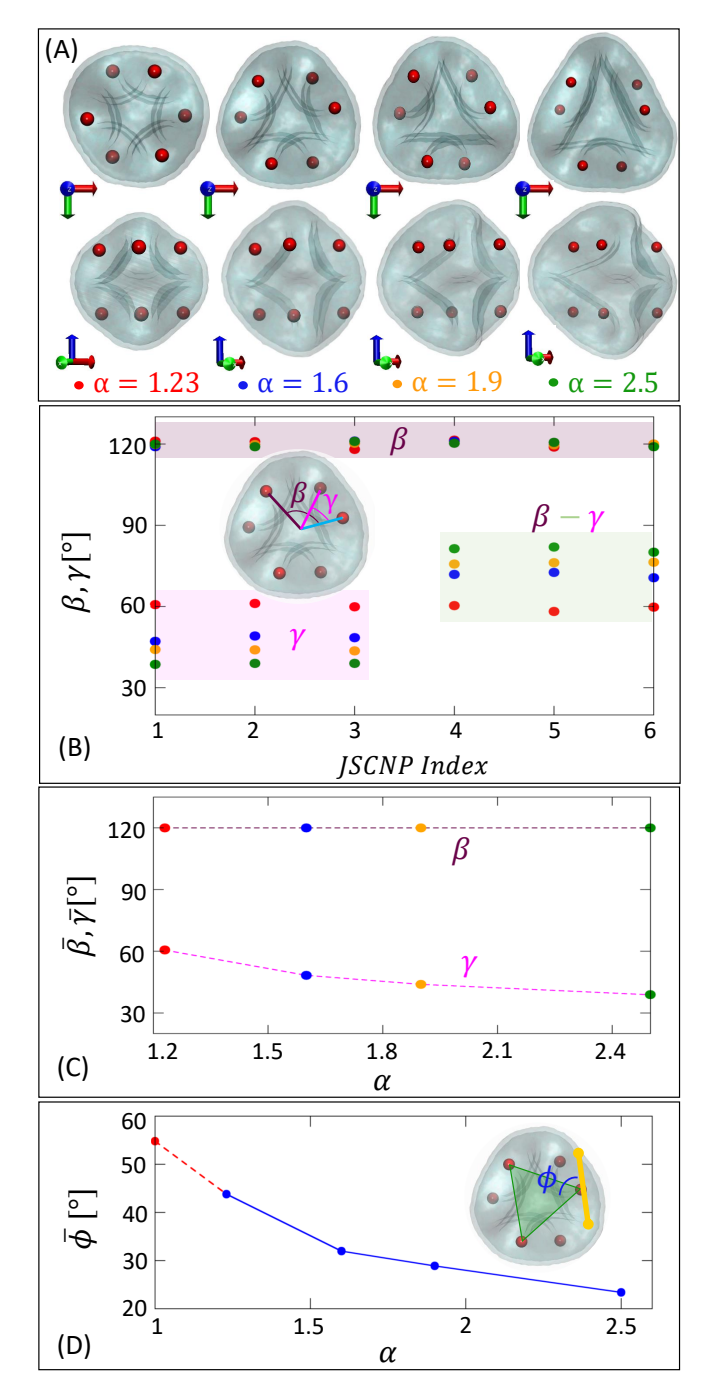


Figure 6: (A) Projected views of the structures shown Centers of JSCNPs in the case of n=6, for all α s shown in 3. This view projects the structure as a 2D structure. (B) Angles, θ , between the projected centers of JSCNP with their first nearest neighbor (γ) and their second nearest neighbor in a counter-clockwise direction (β) for the systems in (A). Inset of (B) schematically defines the angles β and γ . (C) Average values of β and γ as a function of α . (D) Average of the angle ϕ between the orientation of a JSCNP and the plane containing the centers. Note that the value of ϕ converges to 55°, which is the theoretical value in the case where the centers of the JSCNPs form a regular octahedron, the vesicle has the geometry of a cube, and the JSCNPs axes are parallel to the edges of the cube.

Fig. 5(D) shows that the amplitude of the fluctuations of the relative orientations of the JSCNPs, in the case of n = 6, decreases with increasing α , again similar to the case of 4 JSCNPs. This figure demonstrates that, for $\alpha = 2.5$, any arbitrary JSCNP of the nanocluster is almost parallel to one of the other five JSCNPs (blue curve in Fig. 5(D)), while the angles with the other four JSCNPs are high (black, green, red, and orange curves in Fig. 5(D)). This is also demonstrated by Fig. 4(B) (blue curve for n = 6). Namely, the angle of three pairs of JSCNPs is relatively low, i.e., the JSCNPs in each of the three pairs are almost parallel. However, the angles of the remaining 12 pairs are relatively high. Fig. 5(D) shows that the time dependence of the 4 angles between a JSCNP and the 4 JSCNPs that are not parallel to it can be grouped into two correlated pairs. Namely, the black and green curves are correlated, and the red and orange curves are also correlated. These correlations result from the fact that these 4 JSCNPs are composed of two parallel pairs, as stated above.

Inspection of the 6 JSCNPs' snapshots, in Fig. 3, leads us to conclude that the general geometry of their center beads polyhedra is a triangular gyroprism. This structure is clearly demonstrated by the snapshots in Fig. 6(A), which are rotated to emphasize the three-fold symmetry of their geometry. In these snapshots, only centers of mass of the JSCNPs are shown. This figure shows that the JSCNPs' center beads are arranged into two parallel equilateral triangles. These correspond to the base triangles of the 6-JSCNPs' gyroprism. The equilateral nature of these triangles is demonstrated by the angle $\beta \approx 120^{\circ}$, shown by Fig. 6(B) and (C), regardless of α . Here, the vertex of the angle β is the center of mass of the triangle, as defined schematically by the snapshot in Fig. 6(B). The base triangles of the 6-JSCNPs' gyroprism are offset by an angle γ that is about 60° for low values of α , as shown by Fig. 6(B) and (C), confirming our earlier observation that the nanocluster's geometry at $\alpha = 1.23$ is very close to a regular octahedron. However, the angle γ decreases with increasing aspect ratio, as shown by Fig. 6(C). The change of the structure from a regular octahedron to triangular gyroprism with increasing α is also demonstrated by the emergence of several peaks in the corresponding RDF and BAD, shown respectively in Fig. 4(A) and (C). It is interesting to note that the JSCNPs in each triangular base of the gyroprism form a

chiral structure. However, the orientations of the two chiral structures are opposite. It is also interesting to note that the angle, ϕ , between a JSCNP's axis and the plane of the triangular base, to which it belongs, decreases with increasing α , as demonstrated by Fig. 6(D). Therefore, the JSC-NPs' axes in each triangular base become increasingly coplanar with increasing α . The ordered chiral nanocluster of 6 JSCNPs has a distinct geometry, and to our knowledge, such a structured self-assembled nanocluster has not been observed in earlier studies.

Fig. 3 shows that in the case of n = 7, the JSCNPs' center beads form a pentagonal bipyramid in which the 5 JSCNPs of the pentagonal base are perpendicular to the pentagon's plane and the JSCNPs at the apex and bottom vertices of the polyhedron are parallel to the pentagonal base. Fig. 4(B) shows that for the case of n = 7, 10 of the total 21 angles between JSCNPs' axes are close to zero. These correspond to the angles of the JSCNPs' pairs within the pentagonal base. The angles of 10 other JSCNPs' pairs are close to 90°. These correspond to pairs between the apex or bottom JSCNPs and those in the pentagonal base. However, the value of the angle of one pair is about 50° at $\alpha = 1.23$ and increases with increasing α . This corresponds to the angle between the apex and bottom JSCNPs. Fig. S6 in the Supporting Information shows that the amount of fluctuations of the angle between the apex and bottom JSCNPs, in the case of n = 7, is substantially higher than that of the angles between nearest neighbor JSCNPs shown in Figs. 5(E) and (F). This implies that while the pentagonal base of the nanocluster is fairly rigid, the apex and bottom JSCNPs are orientationally less rigid. This is attributed to the conformational frustration of the JSCNPs at the apex and bottom of the nanocluster since the pentagonal base is not even-fold symmetric.

Fig. 3 shows that 8 JSCNPs form a very interesting and highly ordered nanocluster with general details that are independent of α . Inspection of the second and fourth row of Fig. 3, in the case of n=8, implies that the polyhedron formed by the center beads of 8 JSCNPs corresponds to the digonal gyrobianticupola, and that of the vesicle is the elongated gyrobifastigium (dual of the digonal gyrobianticupola). We recently showed that 8 Janus spherical NPs self-assemble into a polyhedron that is intermediate between the snub disphenoid and square antiprism.⁷⁴ Since the

digonal gyrobianticupola polyhedron is simply a distorted snub disphenoid, it is not surprising that 8 JSCNPs self-assemble into a nanocluster with a digonal gyrobianticupola geometry.

It is interesting to note from the snapshots corresponding to n=8, shown in Fig. 3, that all 8 JSCNPs in the nanocluster are parallel to the same plane. Based on their orientations, the 8 JSCNPs can be divided into two sets of 4, where all JSCNPs belonging to each set are parallel, and their corresponding centers are coplanar. Furthermore, JSCNPs belonging to different sets are perpendicular to each other. This is demonstrated by the angles between the JSCNPs' axes, shown in Fig. 4(B), which are either close to 0 or 90°, regardless of α , but with a degree of fluctuations that decreases with α , as shown by Figs. 5(G) and (H). This results in a nematic order parameter parameter that is practically independent of α , except at very low values of α (Fig. S4). It is also interesting to note that the RDF and BAD of 8 JSCNPs at low values of the aspect ratio ($\alpha=1.23$) are qualitatively different from their spherical Janus NP counterparts, ⁷⁴ despite that the overall geometry of the nanocluster is the same. This is due to the fact that the overall geometry of the nanocluster becomes increasingly oblate with increasing α . Among all systems we considered in this study, the nanoclusters with n=3 and 8 are special in that their structures are fairly independent of α . This is particularly demonstrated by the fact that their respective nematic order parameters are almost independent of the aspect ratio.

Effect of Ratio between Area of Vesicle and Net Area of JSCNPs

The results above were obtained from simulations based on a ratio between the vesicle's area and the JSCNPs' net area $\rho=1.2$. We inferred the effect of this ratio on the geometry of the nanocluster by performing additional simulations for the cases of n=4 and 6 with $\alpha=1.9$ at $\rho=3.6$. Figs. 7(A) and (B) show that a moderate increase in ρ does not substantially affect the geometry of the vesicle and the placement of the JSCNPs' centers of mass. The RDFs of the nanoclusters at $\rho=3.6$ are substantially broader than those at $\rho=1.2$, which indicates an increase in the relative fluctuations of the JSCNPs' positions. However, since the peaks remain well-defined at $\rho=3.6$, the nanocluster based on the positions of the JSCNPs' centers remains

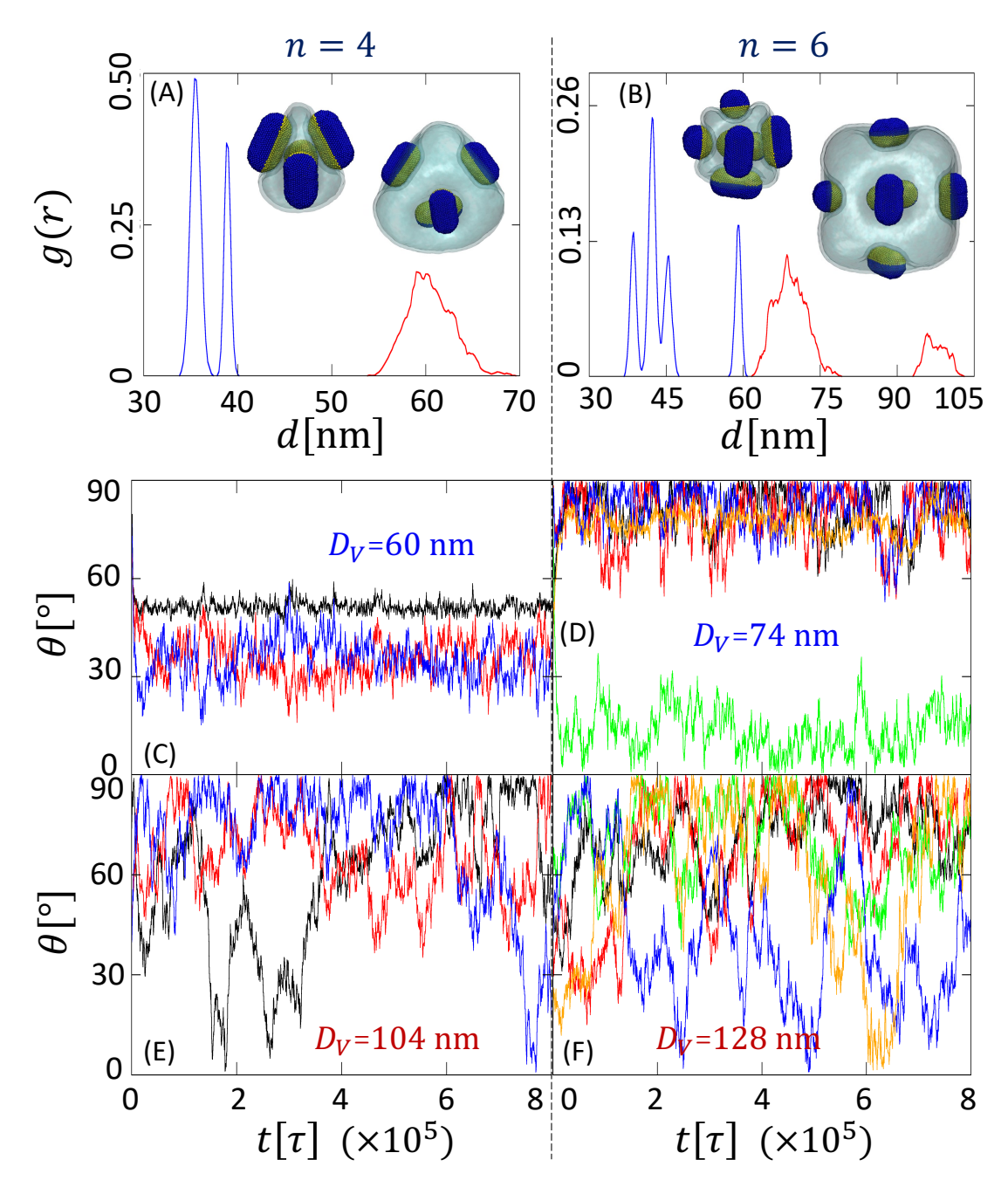


Figure 7: (A) RDF for the case of n=4 and $\alpha=1.9$. Blue and red lines correspond to $\rho=1.2$ and 3.6, respectively. (B) RDF for the case of n=6 and $\alpha=1.9$. Blue and red lines correspond to $\rho=1.2$ and 3.6, respectively. The left and right snapshots in (A) and (B) correspond to $\rho=1.2$ and 3.6, respectively. (C) and (D) Angle θ between the SCNPs' axes versus time in the case of $\rho=1.2$ for n=4 and 6, respectively. (E) and (F) Angle θ between the SCNPs' axes versus time in the case of $\rho=3.6$ for n=4 and 6, respectively.

relatively ordered. Moreover, the fact that the 4-JSCNPs' RDF at $\rho=3.6$ exhibits a single peak instead of two implies that the 4-JSCNPs' nanocluster is closer to a regular tetrahedron than an elongated disphenoid. Likewise, the 6-JSCNPs' nanocluster at $\rho=3.6$ is closer to an octahedron than a triangular gyroprism. Comparison between these results and those shown in Fig. 4(A) implies that increasing vesicle size for a given aspect ratio is, to some extent, equivalent to reducing aspect ratio for a given value of ρ .

The JSCNPs adhering to the larger vesicles also exhibit increased orientational fluctuations with increasing ρ , as demonstrated by the angles of JSCNPs' pairs shown in Figs. 7(C) to (F). Therefore, while the positions of the JSCNPs' positions remain ordered with increasing vesicle size for a given value of α , the JSCNPs' orientations become fluid at high ρ . Therefore, the effect of increasing vesicle size for a given α on the fluctuations of the JSCNPs' orientation is also equivalent to the effect of reducing the aspect ratio for a given value of ρ (see Fig. 5).

Conclusion

The spatial arrangement of Janus spherocylindrical nanoparticles (JSCNPs), which adhere to the outer leaflet of lipid vesicles, is explored through systematic molecular dynamics simulations of an efficient coarse-grained implicit-solvent model. The NPs are longitudinally surface-modified into Janus NPs, such that one moiety interacts more attractively with the lipid head groups than the solvent, while the other moiety interacts more attractively with the solvent than the lipids. This surface modification suppresses endocytosis of the JSCNPs and induces an effective repulsive membrane-curvature-mediated interaction between them.

The central result of the present work is that JSCNPs adhering to lipid vesicles self-assemble into nanoclusters, in which the JSCNPs are apart from each other. These nanoclusters are intricately ordered, with geometries dictated primarily by the number, n, of the JSCNPs on the vesicle and their aspect ratio, α . Highly ordered nanoclusters of spherical Janus NPs adhering to lipid vesicles were observed recently.⁷⁴ However, the present investigation demonstrates that the addition

of a geometric anisotropy feature to the NPs further enriches the diversity of the self-assembled nanostructures. The cample, we found three JSCNPs adhering to a vesicle self-assemble into a nanocluster in which they are parallel to each other, and their centers form an equilateral triangle, regardless of α . The centers of four JSCNPs form a tetrahedron at low values of α , similar to the case of spherical Janus NPs. However, the 4-JSCNPs' polyhedron elongates uniaxially into a disphenoid as α is moderately increased. Likewise, six JSCNPs self-assemble into a regular octahedron at low values of α . However, the structure changes into a triangular gyroprism as α is increased. The JSCNPs become increasingly coplanar in each of the two triangular bases of the gyroprism with increasing α . Eight JSCNPs self-assemble into an interesting polyhedral nanocluster with a geometry corresponding to that of the digonal gyrobiamnticupola. This structure is biaxially anisotropic and becomes increasingly oblate with increasing α . Future experimental studies are warranted to validate our findings.

The nanoclusters observed in the present study are fairly rigid, with a degree of rigidity that increases with the JSCNPs' aspect ratio. Increasing the relative area ρ , which is the ratio between the area of the vesicle and the net area of the JSCNPs, results in increased fluctuations. The effect of increasing ρ for a given α is similar to decreasing α for a given ρ . The rigidity of these structures, coupled with the fact that the nanoclusters are hollow due to the adhesion of the NPs to the vesicle's surface, implies that they may find interesting applications. For example, different placements of the plasmonic spherocylindrical NPs lead to different confinements of photons at the nanoscale and, therefore, allow for modulation of the resonance wavelength.

The present study is based on Janus NPs, which can be fabricated using a variety of experimental methods. ⁸⁵ These include phase separation, ⁸⁶ seed-mediated polymerization, ⁸⁷ microfluidic synthesis, ⁸⁸ masking, ⁸⁹ and nucleation. ⁹⁰ Janus nanorods somewhat similar to the JSCNPs considered in the present study, with Au and polyaniline moieties, were in fact recently synthesized using a droplet-based microfluidic platform. ⁹¹ Janus NPs have a wide range of applications, such as biomedical imaging, ⁹² biosensing, ⁹³ drug delivery, ⁹⁴ cancer therapy, ⁹⁵ and micromechanics. ^{96,97} Nanoassemblies of Janus NPs can find applications in nanophotonics, optical engineering,

and micro/nanomechanics. Nanoassemblies of plasmonic NPs, in particular, exhibit specific optical modes through their localized plasmon resonances. Ordered arrangements of plasmonic NPs, in particular, can exhibit special optical responses, including Fano resonance, ⁹⁸ which has been proven to offer an extremely sensitive sensing capability. The optical response of nanostructured materials is tunable through the geometry and size of the NPs and by the details of their arrangements. Unfortunately, arranging NPs through conventional bottom-up approaches or top-down approaches, including DNA origami, is very challenging. The present study demonstrates that lipid membranes can be used as an alternative approach to self-assemble Janus NPs into fairly rigid nanostructures, both in terms of their positions and their orientations. These conditions are necessary for designing nanostructures with specific optical modes. Future studies to determine the optical modes of the nanostructures observed in this study would be highly desirable.

Methods

The present work is based on a mesoscale implicit-solvent model of self-assembled lipid membranes, 99 in which a lipid molecule is coarse-grained into a short semi-flexible chain that is composed of one hydrophilic head (h) bead and two hydrophobic tail (t) beads. The potential energy of the lipid bilayer has three contributions and is given by,

$$U(\{\mathbf{r}_i\}) = \sum_{i,j} U_0^{\alpha_i \alpha_j}(r_{ij}) + \sum_{\langle i,j \rangle} U_{\text{bond}}^{\alpha_i \alpha_j}(r_{ij}) + \sum_{\langle i,j,k \rangle} U_{\text{bend}}^{\alpha_i \alpha_j \alpha_k}(\mathbf{r}_i, \mathbf{r}_j, \mathbf{r}_k), \tag{1}$$

where \mathbf{r}_i is the coordinate of bead i, $r_{ij} = \mathbf{r}_i - \mathbf{r}_j$, and α_i (= h or t) represents the type of bead i. In Eq. (1), $U_0^{\alpha\beta}$ is a soft two-body potential, between beads of types α and β and is given by

$$U_{0}^{\alpha\beta}(r) = \begin{cases} \left(U_{\max}^{\alpha\beta} - U_{\min}^{\alpha\beta}\right) \frac{(r_{m} - r)^{2}}{r_{m}^{2}} + U_{\min}^{\alpha\beta} & \text{if } r \leq r_{m}, \\ -2 U_{\min}^{\alpha\beta} \frac{(r_{c} - r)^{3}}{(r_{c} - r_{m})^{3}} + 3 U_{\min}^{\alpha\beta} \frac{(r_{c} - r)^{2}}{(r_{c} - r_{m})^{2}} & \text{if } r_{m} < r \leq r_{c}, \\ 0 & \text{if } r > r_{c}, \end{cases}$$
(2)

where $U_{\rm max}^{\alpha\beta}>0$ and $U_{\rm min}^{\alpha\beta}\leq0$ for any pair (α,β) . $U_{\rm min}^{\alpha\beta}=0$ implies a fully repulsive interaction between α and β , and $U_{\rm min}^{\alpha\beta}<0$ implies a short-range attraction between the two beads. The self-assembly of the lipids into thermodynamically stable bilayers is ensured by choosing $U_{\rm min}^{hh}=U_{\rm min}^{ht}=0$ and strong enough negative value of $U_{\rm min}^{tt}$. 99

The second summation in Eq. (1) is over bonded pairs within the lipid chains. The argument of this sum is a harmonic potential that ensures the connectivity of the beads within each chain and is given by

$$U_{\text{bond}}^{\alpha\beta}(r) = \frac{k_{\text{bond}}^{\alpha\beta}}{2} \left(r - a_{\alpha\beta} \right)^2, \tag{3}$$

where $k_{\text{bond}}^{\alpha\beta}$ is the bond stiffness coefficient and $a_{\alpha\beta}$ is the preferred length of the spring. Note that a pair of connected beads within a lipid chain experiences both two-body interaction given by Eq. (S1) in the Supporting Information and bonding interaction given by Eq. (3).

The third summation in Eq. (1) is over the triplets of beads constituting each lipid chain. The argument of this sum is a three-body potential that provides bending stiffness to the lipid chains and is given by

$$U_{\text{bend}}^{\alpha\beta\gamma} \left(\mathbf{r}_{i}, \mathbf{r}_{j}, \mathbf{r}_{k} \right) = \frac{k_{\text{bend}}^{\alpha\beta\gamma}}{2} \left(\cos \varphi_{0}^{\alpha\beta\gamma} - \frac{\mathbf{r}_{ij} \cdot \mathbf{r}_{kj}}{r_{ij} r_{kj}} \right)^{2}, \tag{4}$$

where $k_{\rm bend}^{\alpha\beta\gamma}$ is the bending stiffness coefficient, and $\phi_0^{\alpha\beta\gamma}$ is the preferred splay angle of a lipid chain taken to be 180° .

A spherocylindrical NP of diameter D_N and length $l = \alpha D_N$, where α is its aspect ratio, is constructed as a highly rigid triangulated mesh, with vertices occupied by beads of type p, following the details provided in Section S1 in the Supporting Information. We recently used this NP model to investigate the adhesion modes of spherical NPs^{73,74} and spherocylindrical NPs. ^{46,50} The advantage of this model lies in the fact that the NPs are hollow, which leads to a significant reduction in the number of degrees of freedom associated with the NPs as opposed to models in which NPs are constructed from a three-dimensional arrangement of beads in some lattice structure. ^{44,100} This model allows for simulations of relatively large and many NPs. Every p-bead of the SCNP is connected to its nearest neighbors by the harmonic potential given by Eq. (3), with a

bond stiffness k_{bond}^{pp} and a preferred bond length a_{pp} . Since a SCNP is hollow in this model, the bonding interaction is insufficient to provide high rigidity to the NP. This problem is overcome by introducing an additional bead, c, at the center of mass of the SCNP that is connected to all p-beads by a harmonic bond given by Eq. (3), with a bond stiffness k_{bond}^{cp} and a preferred bond length depending on the location of the p-bead on the spherocylinder.

In the present study, we consider SCNPs that are surface-modified into Janus SCNPs (JSCNPs), such that the plane containing the boundary between its two moieties is parallel to the SCNP's axis, as shown by Fig. S2 in the Supporting Information. A JSCNP is comprised of two types of beads. These correspond to p_a -beads, which interact attractively with the h-beads, and p_b -beads, which interact repulsively with the h-beads. Both p_a - and p_b -beads interact repulsively with t-beads. The two-body potential, $U_0^{\alpha_i\alpha_j}$, given by Eq. (S1) in the Supporting Information, is used for the interaction between the p_a - and p_b -beads with the h- and t-beads, with $U_{\min}^{p_ah} < 0$ and $U_{\min}^{p_bh} = U_{\min}^{p_at} = U_{\min}^{p_at} = 0$. Beads belonging to different JSCNPs interact with each other via the same two-body potential $U_0^{\alpha_i\alpha_j}$, given by Eq. (S1) in the Supporting Information. This interaction is chosen to be entirely repulsive ($U_{\min}^{p_ap_a} = U_{\min}^{p_bp_b} = U_{\min}^{p_ap_b} = 0$) to prevent the JSCNPs from aggregation in the absence of lipid membranes. The adhesion energy density is defined as $\xi = |U_{adh}|/A_{adh}$, where U_{adh} is the net potential energy between the NP and the membrane, and A_{adh} is the area of the NP adhering to the membrane. Details of the calculation of ξ are found in Refs. 46,73

All beads are moved using a molecular dynamics scheme with a Langevin thermostat, 101

$$\dot{\mathbf{r}}_i(t) = \mathbf{v}_i(t) \tag{5}$$

$$m\dot{\mathbf{v}}_i(t) = -\nabla_i U(\{\mathbf{r}_i\}) - \Gamma \mathbf{v}_i(t) + \sigma \Xi_i(t),$$
 (6)

where m is the mass of a bead (same for all beads), Γ is the friction coefficient, and $\sigma\Xi_i(t)$ is a random force originating from the heat bath. $\Xi_i(t)$ is a random vector generated from a uniform distribution and obeys $\langle \Xi_i(t) \rangle = 0$ and $\langle \Xi_i^{(\mu)}(t)\Xi_j^{(\nu)}(t') \rangle = \delta_{\mu\nu}\delta_{ij}\delta(t-t')$, where μ and $\nu = x, y$ or z. The dissipative and random forces are interrelated through the fluctuation-dissipation theorem,

Table 1: Model parameters

Parameter	Value
$U_{ m max}^{hh}, U_{ m max}^{ht}$	100ε
$U_{ m max}^{tt}$	200ε
$U_{ m min}^{hh},U_{ m min}^{ht}$	0
$U_{ m min}^{tt}$	-6ε
$U_{ m max}^{p_ah}$	200ε
$U_{ m min}^{p_a h}$	-4ε
$U_{ m max}^{p_bh}, U_{ m max}^{p_bt}, U_{ m max}^{p_at}$	100ε
$U_{\min}^{p_bh}, U_{\min}^{p_bt}, U_{\min}^{p_at}$	0
$U_{ m max}^{p_ap_a}, U_{ m max}^{p_ap_b}, U_{ m max}^{p_bp_b}$	200ε
$U_{\min}^{p_ap_a}, U_{\min}^{p_ap_b}, U_{\min}^{p_bp_b}$	0
$k_{\mathrm{bond}}^{ht}, k_{\mathrm{bond}}^{tt}$	$100\varepsilon/r_m^2$
k ^{htt} bend	100ε
$k_{\text{bond}}^{p_a p_a}, k_{\text{bond}}^{p_a p_b}, k_{\text{bond}}^{p_b p_b}$	$500\varepsilon/r_m^2$
$k_{\text{bond}}^{p_a c}, k_{\text{bond}}^{p_b c}$	$10\varepsilon/r_m^2$
r_c	$2r_m$
a_{ht}, a_{tt}	$0.7r_m$
a_{cp_a}, a_{cp_b}	variable

which leads to $\Gamma = \sigma^2/2k_BT$. Eqs. (5) and (6) are integrated numerically using the velocity-Verlet algorithm 102 with $\Gamma = \sqrt{6}m/\tau$ and a time step $\Delta t = 0.02\tau$, where $\tau = r_m(m/\epsilon)^{1/2}$.

Table 1 gives the values of the model's interaction parameters. In all simulations, the JSCNPs diameter $D_N=20\,r_m$. Their aspect ratio, α , varies between 1.23 and 5.5. All simulations are executed at $k_BT=3.0\varepsilon$. With the parameters in Table 1, the adhesion energy of the JSCNP on the membrane per unit of contact area, is $\xi=4.11\,k_BT/r_m^2$. The bending modulus of the bare bilayer, with the interaction parameters shown in Table 1, as extracted from the spectrum of the height fluctuations of the bilayer, is $\kappa\approx30\,k_BT$, ⁴⁴ comparable to that of a DPPC bilayer in the fluid phase. ¹⁰³ By comparing the thickness of this model bilayer in the fluid phase, which is about $4\,r_m$, with that of a typical fluid phospholipid bilayer, which is about $4\,\mathrm{nm}$, ¹⁰⁴ we estimate $r_m\approx1\,\mathrm{nm}$. Hence, in the remainder of this article, lengths and the adhesion energy density, ξ , are expressed in units of nanometers and k_BT/nm^2 , respectively.

The simulations are performed on vesicles with a diameter, D_V , ranging between 48 and 160 nm. Here, D_V is defined as twice the average distance between the positions of the h-beads of the outer leaflet and the vesicle's center of mass. This corresponds to a total number of lipid chains in a vesicle ranging between 2.5×10^4 and 3.2×10^5 . The fraction of a JSCNP's area that adheres to the membrane is fixed at J = 0.4. In a typical simulation, n JSCNPs, initially placed close to an equilibrated vesicle at random positions, quickly adhere to the vesicle. We consider values of n corresponding to 3, 4, 6, 7, and 8. Unless indicated, the ratio $\rho = A_V/nA_N = 1.2$ in all simulations, where A_V is the surface area of the outer leaflet of the vesicle and A_N is the surface area of a single JSCNP. Most simulations were run over 4×10^7 time steps. Typically, systems are equilibrated over $2 \times 10^5 \tau$. We emphasize that the results presented in this article are independent of the initial conditions. Therefore, quantities, such as the radial distribution functions (RDF), bond angle distributions (BADs), and angles between the axes of the JSCNPs, for a specific set of parameters, are calculated from averaging over a long interval of time after equilibration, typically ranging between $4 \times 10^5 \tau$ and $8 \times 10^5 \tau$.

Acknowledgements

This work was supported by a grant from the National Science Foundation (DMR-1931837). The simulations were performed on computers of the University of Memphis High Performance Computing. Snapshots in this article were generated using VMD version 1.9.3. ¹⁰⁵

Supporting Information

Numerical construction of a spherocylindrical NP; Construction of a Janus spherocylindrical NP (JSCNP); Distance between two JSCNPs vs. time in the case of $\alpha = 1.6$; Equilibrium nanocluster composed of five JSCNPs with $\alpha = 1.9$; Nematic order parameter vs. α ; Biased interaction in the case of four JSCNPs; Adhesion and curvature energies vs. time in the case of four JSCNPs with and without bias; Curvature energy calculation; Angle between JSCNPs, at the poles of a seven-JSCNPs nanocluster, vs. time for the cases of $\alpha = 1.23$ and 2.5

Competing interests

The authors declare no competing interests.

References

- (1) Singamaneni, S.; Bliznyuk, V. N.; Binek, C.; Tsymbal, E. Y. Magnetic Nanoparticles: Recent Advances in Synthesis, Self-Assembly and Applications. *J. Mat. Chem.* **2011**, *21*, 16819–16845.
- (2) Jiang, C.; Leung, C. W.; Pong, P. W. T. Magnetic-Field-Assisted Assembly of Anisotropic Superstructures by Iron Oxide Nanoparticles and Their Enhanced Magnetism. *Nanoscale Res. Lett.* **2016**, *11*, 189.

- (3) Yu, Z.; Tetard, L.; Zhai, L.; Thomas, J. Supercapacitor electrode materials: nanostructures from 0 to 3 dimensions. *Energy Environ. Sci.* **2015**, *8*, 702–730.
- (4) Kundu, S.; Patra, A. Nanoscale Strategies for Light Harvesting. *Chem. Rev.* **2017**, *117*, 712–757.
- (5) Lamarre, J.-M.; Billard, F.; Kerboua, C. H.; Lequime, M.; Roorda, S.; Martinu, L. Anisotropic Nonlinear Optical Absorption of Gold Nanorods in a Silica Matrix. *Opt. Commun.* 2008, 281, 331–340.
- (6) Yang, A.; Hoang, T. B.; Dridi, M.; Deeb, C.; Mikkelsen, M. H.; Schatz, G. C.; Odom, T. W. Real-Time Tunable Lasing from Plasmonic Nanocavity Arrays. *Nat. Commun.* 2015, 6, 6939.
- (7) Yu, C.; Guo, X.; Shen, M.; Shen, B.; Muzzio, M.; Yin, Z.; Li, Q.; Xi, Z.; Li, J.; Seto, C. T.; Sun, S. Maximizing the Catalytic Activity of Nanoparticles through Monolayer Assembly on Nitrogen-Doped Graphene. *Angew. Chem. Int. Ed.* **2018**, *57*, 451–455.
- (8) Bian, T.; Gardin, A.; Gemen, J.; Houben, L.; Perego, C.; Lee, B.; Elad, N.; Chu, Z.; Pavan, G. M.; Klajn, R. Electrostatic Co-Assembly of Nanoparticles with Oppositely Charged Small Molecules into Static and Dynamic Superstructures. *Nat. Chem.* 2021, 13, 940–949.
- (9) Wang, L.; Xu, L.; Kuang, H.; Xu, C.; Kotov, N. A. Dynamic Nanoparticle Assemblies. *Acc. Chem. Res.* **2012**, *45*, 1916–1926.
- (10) Janib, S. M.; Moses, A. S.; MacKay, J. A. Imaging and Drug Delivery Using Theranostic Nanoparticles. *Adv. Drug Deliv. Rev.* **2010**, *62*, 1052–1063.
- (11) Wu, X.; Hao, C.; Kumar, J.; Kuang, H.; Kotov, N. A.; Liz-Marzán, L. M.; Xu, C. Environmentally Responsive Plasmonic Nanoassemblies for Biosensing. *Chem. Soc. Rev.* 2018, 47, 4677–4696.

- (12) Kim, W.-G.; Lee, J.-M.; Yang, Y.; Kim, H.; Devaraj, V.; Kim, M.; Jeong, H.; Choi, E.-J.; Yang, J.; Jang, Y.; Badloe, T.; Lee, D.; Rho, J.; Kim, J. T.; Oh, J.-W. Three-Dimensional Plasmonic Nanocluster-Driven Light–Matter Interaction for Photoluminescence Enhancement and Picomolar-Level Biosensing. *Nano Lett.* 2022, 22, 4702–4711.
- (13) Pissuwan, D.; Niidome, T.; Cortie, M. B. The Forthcoming Applications of Gold Nanoparticles in Drug and Gene Delivery Systems. *J. Control Release* **2011**, *149*, 65–71.
- (14) Sarkar, A. K.; Debnath, K.; Arora, H.; Seth, P.; Jana, N. R.; Jana, N. R. Direct Cellular Delivery of Exogenous Genetic Material and Protein via Colloidal Nano-Assemblies with Biopolymer. ACS Appl. Mater. Interfaces 2022, 14, 3199–3206.
- (15) Wang, Y.; Mirkin, C. A.; Park, S.-J. Nanofabrication beyond electronics. *ACS Nano* **2009**, 3, 1049–1056, PMID: 19845365.
- (16) Lee, H.-B.-R.; Bent, S. F. A selective toolbox for nanofabrication. *Chem. Mater.* **2020**, *32*, 3323–3324.
- (17) Chai, Z.; Childress, A.; Busnaina, A. A. Directed assembly of nanomaterials for making nanoscale devices and structures: Mechanisms and applications. *ACS Nano* **2022**, *16*, 17641–17686, PMID: 36269234.
- (18) Lin, T.-C.; Cao, C.; Sokoluk, M.; Jiang, L.; Wang, X.; Schoenung, J. M.; Lavernia, E. J.; Li, X. Aluminum with dispersed nanoparticles by laser additive manufacturing. *Nat. Commun.* 2019, 10, 4124.
- (19) Saifullah, M. S. M.; Asbahi, M.; Neo, D. C. J.; Mahfoud, Z.; Tan, H. R.; Ha, S. T.; Dwivedi, N.; Dutta, T.; bin Dolmanan, S.; Aabdin, Z.; Bosman, M.; Ganesan, R.; Tripathy, S.; Hasko, D. G.; Valiyaveettil, S. Patterning at the Resolution Limit of Commercial Electron Beam Lithography. *Nano Lett.* 2022, 22, 7432–7440.

- (20) Li, P.; Chen, S.; Dai, H.; Yang, Z.; Chen, Z.; Wang, Y.; Chen, Y.; Peng, W.; Shan, W.; Duan, H. Recent advances in focused ion beam nanofabrication for nanostructures and devices: fundamentals and applications. *Nanoscale* **2021**, *13*, 1529–1565.
- (21) Kang, H.; Detcheverry, F. A.; Mangham, A. N.; Stoykovich, M. P.; Daoulas, K. C.; Hamers, R. J.; Müller, M.; de Pablo, J. J.; Nealey, P. F. Hierarchical Assembly of Nanoparticle Superstructures from Block Copolymer-Nanoparticle Composites. *Phys. Rev. Lett.* 2008, 100, 148303.
- (22) Mirkin, C. A.; Letsinger, R. L.; Mucic, R. C.; Storhoff, J. J. A DNA-Based Method for Rationally Assembling Nanoparticles into Macroscopic Materials. *Nature* **1996**, *382*, 607–609.
- (23) Rothemund, P. W. Folding DNA to Create Nanoscale Shapes and Patterns. *Nature* **2006**, 440, 297–302.
- (24) Tian, Y.; Wang, T.; Liu, W.; Xin, H. L.; Li, H.; Ke, Y.; Shih, W. M.; Gang, O. Prescribed Nanoparticle Cluster Architectures and Low-Dimensional Arrays Built Using Octahedral DNA Origami Frames. *Nat. Nanotechnol.* 2015, 10, 637–644.
- (25) Urban, M. J.; Dutta, P. K.; Wang, P.; Duan, X.; Shen, X.; Ding, B.; Ke, Y.; Liu, N. Plasmonic Toroidal Metamolecules Assembled by DNA Origami. *J. Am. Chem. Soc.* **2016**, *138*, 5495–5498.
- (26) Veneziano, R.; Ratanalert, S.; Zhang, K.; Zhang, F.; Yan, H.; Chiu, W.; Bathe, M. Designer Nanoscale DNA Assemblies Programmed from the Top Down. *Science* **2016**, *352*, 1534–1534.
- (27) Cecconello, A.; Kahn, J. S.; Lu, C.-H.; Khosravi Khorashad, L.; Govorov, A. O.; Willner, I. DNA Scaffolds for the Dictated Assembly of Left-/Right-Handed Plasmonic Au NP Helices with Programmed Chiro-Optical Properties. J. Am. Chem. Soc. 2016, 138, 9895–9901.

- (28) Stevens, M. M.; Flynn, N. T.; Wang, C.; Tirrell, D. A.; Langer, R. Coiled-Coil Peptide-Based Assembly of Gold Nanoparticles. *Adv. Mat.* **2004**, *16*, 915–918.
- (29) Gurunatha, K. L.; Fournier, A. C.; Urvoas, A.; Valerio-Lepiniec, M.; Marchi, V.; Minard, P.; Dujardin, E. Nanoparticles Self-Assembly Driven by High Affinity Repeat Protein Pairing. ACS Nano 2016, 10, 3176–3185.
- (30) Tian, H.; He, J. Cellulose as a Scaffold for Self-Assembly: From Basic Research to Real Applications. *Langmuir* **2016**, *32*, 12269–12282.
- (31) Fan, Y.; Liu, Y.; Wu, Y.; Dai, F.; Yuan, M.; Wang, F.; Bai, Y.; Deng, H. Natural Polysaccharides Based Self-Assembled Nanoparticles for Biomedical Applications -A Review. *Int. J. Biol. Macromol.* **2021**, *192*, 1240–1255.
- (32) Lin, G.; Chee, S. W.; Raj, S.; Král, P.; Mirsaidov, U. Linker-Mediated Self-Assembly Dynamics of Charged Nanoparticles. *ACS Nano* **2016**, *10*, 7443–7450.
- (33) Rahimi, M.; Roberts, T. F.; Armas-Pérez, J. C.; Wang, X.; Bukusoglu, E.; Abbott, N. L.; de Pablo, J. J. Nanoparticle Self-Assembly at the Interface of Liquid Crystal Droplets. *Proc. Natl. Acad. Sci. U. S. A.* **2015**, *112*, 5297–5302.
- (34) Kühler, P.; Roller, E.-M.; Schreiber, R.; Liedl, T.; Lohmüller, T.; Feldmann, J. Plasmonic DNA-Origami Nanoantennas for Surface-Enhanced Raman Spectroscopy. *Nano Lett.* 2014, 14, 2914–2919.
- (35) Roller, E.-M.; Besteiro, L. V.; Pupp, C.; Khorashad, L. K.; Govorov, A. O.; Liedl, T. Hotspot-mMediated Non-Dissipative and Ultrafast Plasmon Passage. *Nat. Phys.* **2017**, *13*, 761–765.
- (36) Pilo-Pais, M.; Watson, A.; Demers, S.; LaBean, T. H.; Finkelstein, G. Surface-Enhanced Raman Scattering Plasmonic Enhancement Using DNA Origami-Based Complex Metallic Nanostructures. *Nano Lett.* 2014, 14, 2099–2104.

- (37) Matsuura, K.; Ueno, G.; Fujita, S. Self-Assembled Artificial Viral Capsid Decorated with Gold Nanoparticles. *Polym. J.* **2015**, *47*, 146–151.
- (38) Xu, L.; Yan, W.; Ma, W.; Kuang, H.; Wu, X.; Liu, L.; Zhao, Y.; Wang, L.; Xu, C. SERS Encoded Silver Pyramids for Attomolar Detection of Multiplexed Disease Biomarkers. *Adv. Mat.* **2015**, *27*, 1706–1711.
- (39) Chen, W.; Bian, A.; Agarwal, A.; Liu, L.; Shen, H.; Wang, L.; Xu, C.; Kotov, N. A. Nanoparticle Superstructures Made by Polymerase Chain Reaction: Collective Interactions of Nanoparticles and a New Principle for Chiral Materials. *Nano Lett.* **2009**, *9*, 2153–2159.
- (40) Shen, X.; Asenjo-Garcia, A.; Liu, Q.; Jiang, Q.; García de Abajo, F. J.; Liu, N.; Ding, B. Three-Dimensional Plasmonic Chiral Tetramers Assembled by DNA Origami. *Nano Lett.* 2013, 13, 2128–2133.
- (41) Jiang, Q.; Liu, Q.; Shi, Y.; Wang, Z.-G.; Zhan, P.; Liu, J.; Liu, C.; Wang, H.; Shi, X.; Zhang, L.; Sun, J.; Ding, B.; Liu, M. Stimulus-Responsive Plasmonic Chiral Signals of Gold Nanorods Organized on DNA Origami. *Nano Lett.* 2017, 17, 7125–7130.
- (42) Mouritsen, O. G. Life As a Matter of Fat; Springer, 2005.
- (43) Deserno, M.; Gelbart, W. M. Adhesion and Wrapping in Colloid-Vesicle Complexes. *J. Phys. Chem. B* **2002**, *106*, 5543–5552.
- (44) Spangler, E. J.; Upreti, S.; Laradji, M. Partial Wrapping and Spontaneous Endocytosis of Spherical Nanoparticles by Tensionless Lipid Membranes. *J. Chem. Phys.* **2016**, *144*, 044901.
- (45) Spangler, E. J.; Laradji, M. Discontinuous Wrapping Transition of Spherical Nanoparticles by Tensionless Lipid Membranes. *J. Chem. Phys.* **2020**, *152*, 104902.
- (46) Sharma, A.; Zhu, Y.; Spangler, E. J.; Laradji, M. Modes of Adhesion of Spherocylindrical Nanoparticles to Tensionless Lipid Bilayers. *J. Chem. Phys.* **2022**, *156*, 234901.

- (47) Reynwar, B. J.; Illya, G.; Harmandaris, V. A.; Müller, M. M.; Kremer, K.; Deserno, M. Aggregation and Vesiculation of Membrane Proteins by Curvature-Mediated Interactions. *Nature* **2007**, *447*, 461–464.
- (48) Bahrami, A. H.; Lipowsky, R.; Weikl, T. R. Tubulation and Aggregation of Spherical Nanoparticles Adsorbed on Vesicles. *Phys. Rev. Lett.* **2012**, *109*, 188102.
- (49) Spangler, E. J.; Laradji, M. Spatial Arrangements of Spherical Nanoparticles on Lipid Vesicles. *J. Chem. Phys.* **2021**, *154*, 244902.
- (50) Sharma, A.; Zhu, Y.; Spangler, E. J.; Carrillo, J.-M. Y.; Laradji, M. Membrane-Mediated Dimerization of Spherocylindrical Nanoparticles. *Soft Matter* **2023**, *19*, 1499–1512.
- (51) Ramos, L.; Lubensky, T.; Nelson, P.; Weitz, D. I. Surfactant-Mediated Two-Dimensional Crystallization of Colloidal Crystals. *Science* **1999**, 286, 2325–2328.
- (52) Koltover, I.; R\u00e4dler, J. O.; Safinya, C. R. Membrane Mediated Attraction and Ordered Aggregation of Colloidal Particles Bound to Giant Phospholipid Vesicles. *Phys. Rev. Lett.* 1999, 82, 1991–1994.
- (53) Xi, A.; Bothun, G. D. Centrifugation-Based Assay for Examining Nanoparticle-Lipid Membrane Binding and Disruption. *Analyst* **2014**, *139*, 973–981.
- (54) Hickey, R. J.; Koski, J.; Meng, X.; Riggleman, R. A.; Zhang, P.; Park, S.-J. Size-Controlled Self-Assembly of Superparamagnetic Polymersomes. *ACS Nano* **2014**, *8*, 495–502.
- (55) van der Wel, C.; Vahid, A.; Šarić, A.; Idema, T.; Heinrich, D.; Kraft, D. J. Lipid Membrane-Mediated Attraction between Curvature Inducing Objects. *Sci. Rep.* **2016**, *6*, 32825.
- (56) Sugikawa, K.; Kadota, T.; Yasuhara, K.; Ikeda, A. Anisotropic Self-Assembly of Citrate-Coated Gold Nanoparticles on Fluidic Liposomes. *Angew. Chem. Int. Ed.* **2016**, *55*, 4059–4063.

- (57) Jena, P.; Bhattacharya, M.; Bhattacharjee, G.; Satpati, B.; Mukherjee, P.; Senapati, D.; Srinivasan, R. Bimetallic Gold-Silver Nanoparticles Mediate Bacterial Killing by Disrupting the Actin Cytoskeleton MreB. *Nanoscale* **2020**, *12*, 3731–3749.
- (58) Liu, X.; Auth, T.; Hazra, N.; Ebbesen, M. F.; Brewer, J.; Gompper, G.; Crassous, J. J.; Sparr, E. Wrapping Anisotropic Microgel Particles in Lipid Membranes: Effects of Particle Shape and Membrane Rigidity. *Proc. Natl. Acad. Sci. U.S.A.* **2023**, *120*, e2217534120.
- (59) Smith, K. A.; Jasnow, D.; Balazs, A. C. Designing Synthetic Vesicles that Engulf Nanoscopic Particles. *J. Chem. Phys.* **2007**, *127*, 08B612.
- (60) Šarić, A.; Cacciuto, A. Fluid Membranes Can Drive Linear Aggregation of Adsorbed Spherical Nanoparticles. *Phys. Rev. Lett.* **2012**, *108*, 118101.
- (61) Šarić, A.; Cacciuto, A. Mechanism of Membrane Tube Formation Induced by Adhesive Nanocomponents. *Phys. Rev. Lett.* **2012**, *109*, 188101.
- (62) Reynwar, B. J.; Deserno, M. Membrane-Mediated Interactions between Circular Particles in the Strongly Curved Regime. *Soft Matter* 2011, 7, 8567–8575.
- (63) Yang, K.; Ma, Y.-Q. Computer Simulation of the Translocation of Nanoparticles with Different Shapes Across a Lipid Bilayer. *Nat. Nanotechnol.* **2010**, *5*, 579–583.
- (64) Spangler, E. J.; Kumar, P. B. S.; Laradji, M. Stability of Membrane-Induced Self-Assemblies of Spherical Nanoparticles. *Soft Matter* **2018**, *14*, 5019–5030.
- (65) Azadbakht, A.; Meadowcroft, B.; Májek, J.; Šarić, A.; Kraft, D. J. Nonadditivity in interactions between three membrane-wrapped colloidal spheres. *Biophys. J.* **2024**, *123*, 307–316.
- (66) Sarfati, R.; Dufresne, E. R. Long-range attraction of particles adhered to lipid vesicles. *Phys. Rev. E* **2016**, *94*, 012604.

- (67) Xiong, K.; Zhao, J.; Yang, D.; Cheng, Q.; Wang, J.; Ji, H. Cooperative Wrapping of Nanoparticles of Various Sizes and Shapes by Lipid Membranes. *Soft Matter* **2017**, *13*, 4644–4652.
- (68) Petrova, A. B.; Herold, C.; Petrov, E. P. Conformations and membrane-driven self-organization of rodlike fd virus particles on freestanding lipid membranes. *Soft Matter* **2017**, *13*, 7172–7187.
- (69) Percebom, A. M.; Costa, L. H. M. Formation and Assembly of Amphiphilic Janus Nanoparticles Promoted by Polymer Interactions. *Adv. Colloid Interface Sci.* **2019**, 269, 256–269.
- (70) Kim, M.; Jeon, K.; Hee Kim, W.; Wook Lee, J.; Hwang, Y.-H.; Lee, H. Biocompatible Amphiphilic Janus Nanoparticles with Enhanced Interfacial Properties for Colloidal Surfactants. J. Colloid Interface Sci. 2022, 616, 488–498.
- (71) Agudo-Canalejo, J.; Lipowsky, R. Uniform and Janus-like nanoparticles in contact with vesicles: energy landscapes and curvature-induced forces. *Soft Matter* **2017**, *13*, 2155–2173.
- (72) Bahrami, A. H.; Weikl, T. R. Curvature-Mediated Assembly of Janus Nanoparticles on Membrane Vesicles. *Nano Lett.* **2018**, *18*, 1259–1263.
- (73) Zhu, Y.; Sharma, A.; Spangler, E. J.; Laradji, M. Modes of Adhesion of Two Janus Nanoparticles on the Outer or Inner Side of Lipid Vesicles. *Soft Matter* **2022**, *18*, 4689–4698.
- (74) Zhu, Y.; Sharma, A.; Spangler, E. J.; Carrillo, J.-M. Y.; Kumar, P. S.; Laradji, M. Lipid Vesicles Induced Ordered Nanoassemblies of Janus Nanoparticles. *Soft Matter* 2023, 19, 2204–2213.
- (75) Zhu, Y.; Sharma, A.; Spangler, E. J.; Laradji, M. Non-Close-Packed Hexagonal Self-Assembly of Janus Nanoparticles on Planar Membranes. *Soft Matter* **2023**, *19*, 7591–7601.
- (76) Dhand, C.; Dwivedi, N.; Loh, X. J.; Jie Ying, A. N.; Verma, N. K.; Beuerman, R. W.; Lakshminarayanan, R.; Ramakrishna, S. Methods and Strategies for the Synthesis of Di-

- verse Nanoparticles and their Applications: A Comprehensive Overview. *RSC Adv.* **2015**, *5*, 105003–105037.
- (77) Xia, Y.; Chen, Q.; Banin, U. Introduction: Anisotropic Nanomaterials. *Chem. Rev.* **2023**, 123, 3325–3328.
- (78) Weikl, T. R. Indirect interactions of membrane-adsorbed cylinders. *The European Physical Journal E* **2003**, *12*, 265–273.
- (79) Wu, Z.; Yi, X. Membrane-mediated interaction of intercellular cylindrical nanoparticles. *Phys. Rev. E* **2021**, *104*, 034403.
- (80) Kumar, S.; Rosenberg, J. M.; Bouzida, D.; Swendsen, R. H.; Kollman, P. A. The Weighted Histogram Analysis Method for Free-Energy Calculations on Biomolecules. I. The method. *J. Comp. Chem.* **1992**, *13*, 1011–1021.
- (81) Torrie, G.; Valleau, J. Nonphysical Sampling Distributions in Monte Carlo Free-energy Estimation: Umbrella Sampling. *J. Comp. Phys.* **1977**, *23*, 187–199.
- (82) Eppenga, R.; Frenkel, D. Monte Carlo Study of the Isotropic and Nematic Phases of Infinitely Thin Hard Platelets. *Mol. Phys.* **1984**, *52*, 1303–1334.
- (83) Caroli, M.; de Castro, P. M. M.; Loriot, S.; Rouiller, O.; Teillaud, M.; Wormser, C. Robust and Efficient Delaunay Triangulations of Points on Or Close to a Sphere. Experimental Algorithms. Berlin, Heidelberg, 2010; pp 462–473.
- (84) Helfrich, W. Elastic Properties of Lipid Bilayers: Theory and Possible Experiments. *Z. Naturforsch. C* **1973**, 28, 693–703.
- (85) Safaie, N.; Ferrier, J., Robert C. Janus nanoparticle synthesis: Overview, recent developments, and applications. *J. Appl. Phys.* **2020**, *127*, 170902.

- (86) Zhang, Y.; Kang, L.; Huang, H.; Deng, J. Optically Active Janus Particles Constructed by Chiral Helical Polymers through Emulsion Polymerization Combined with Solvent Evaporation-Induced Phase Separation. *ACS Appl. Mater. Interfaces* **2020**, *12*, 6319–6327.
- (87) Liu, B.; Wei, W.; Qu, X.; Yang, Z. Janus Colloids Formed by Biphasic Grafting at a Pickering Emulsion Interface. *Angewandte Chemie International Edition* **2008**, *47*, 3973–3975.
- (88) Roh, K.-H.; Yoshida, M.; Lahann, J. Water-Stable Biphasic Nanocolloids with Potential Use as Anisotropic Imaging Probes. *Langmuir* **2007**, *23*, 5683–5688.
- (89) Mou, F.; Chen, C.; Zhong, Q.; Yin, Y.; Ma, H.; Guan, J. Autonomous Motion and Temperature-Controlled Drug Delivery of Mg/Pt-Poly(N-isopropylacrylamide) Janus Micromotors Driven by Simulated Body Fluid and Blood Plasma. *ACS Appl. Mater. Interfaces* **2014**, *6*, 9897–9903.
- (90) Choi, S.-H.; Na, H. B.; Park, Y. I.; An, K.; Kwon, S. G.; Jang, Y.; Park, M.-h.; Moon, J.; Son, J. S.; Song, I. C.; Moon, W. K.; Hyeon, T. Simple and Generalized Synthesis of OxideMetal Heterostructured Nanoparticles and their Applications in Multimodal Biomedical Probes. J. Am. Chem. Soc. 2008, 130, 15573–15580.
- (91) Wang, Y.; Shang, M.; Wang, Y.; Xu, Z. Droplet-based microfluidic synthesis of (Au nanorod@Ag)-polyaniline Janus nanoparticles and their application as a surface-enhanced Raman scattering nanosensor for mercury detection. *Anal. Methods* **2019**, *11*, 3966–3973.
- (92) Zhu, J.; Lu, Y.; Li, Y.; Jiang, J.; Cheng, L.; Liu, Z.; Guo, L.; Pan, Y.; Gu, H. Synthesis of Au–Fe3O4 heterostructured nanoparticles for in vivo computed tomography and magnetic resonance dual model imaging. *Nanoscale* **2014**, *6*, 199–202.
- (93) Wang, Y.; Shang, M.; Wang, Y.; Xu, Z. Droplet-based microfluidic synthesis of (Au nanorod@Ag)-polyaniline Janus nanoparticles and their application as a surface-enhanced Raman scattering nanosensor for mercury detection. *Anal. Methods* **2019**, *11*, 3966–3973.

- (94) Wang, W.; Wang, P.; Chen, L.; Zhao, M.; Hung, C.-T.; Yu, C.; Al-Khalaf, A. A.; Hozzein, W. N.; Zhang, F.; Li, X.; Zhao, D. Engine-Trailer-Structured Nanotrucks for Efficient Nano-Bio Interactions and Bioimaging-Guided Drug Delivery. *Chem* 2020, 6, 1097–1112.
- (95) Lin, X.; Liu, S.; Zhang, X.; Zhu, R.; Chen, S.; Chen, X.; Song, J.; Yang, H. An Ultrasound Activated Vesicle of Janus Au-MnO Nanoparticles for Promoted Tumor Penetration and Sono-Chemodynamic Therapy of Orthotopic Liver Cancer. *Angewandte Chemie International Edition* **2020**, *59*, 1682–1688.
- (96) Maric, T.; Nasir, M. Z. M.; Webster, R. D.; Pumera, M. Tailoring Metal/TiO2 Interface to Influence Motion of Light-Activated Janus Micromotors. *Advanced Functional Materials* 2020, 30, 1908614.
- (97) Zhang, X.; Fu, Q.; Duan, H.; Song, J.; Yang, H. Janus Nanoparticles: From Fabrication to (Bio)Applications. *ACS Nano* **2021**, *15*, 6147–6191.
- (98) King, N. S.; Liu, L.; Yang, X.; Cerjan, B.; Everitt, H. O.; Nordlander, P.; Halas, N. J. Fano Resonant Aluminum Nanoclusters for Plasmonic Colorimetric Sensing. *ACS Nano* **2015**, *9*, 10628–10636.
- (99) Revalee, J. D.; Laradji, M.; Sunil Kumar, P. Implicit-Solvent Mesoscale Model Based on Soft-Core Potentials for Self-Assembled Lipid Membranes. *J. Chem. Phys.* **2008**, *128*, 01B614.
- (100) Vácha, R.; Martinez-Veracoechea, F. J.; Frenkel, D. Receptor-Mediated Endocytosis of Nanoparticles of Various Shapes. *Nano Lett.* **2011**, *11*, 5391–5395.
- (101) Grest, G. S.; Kremer, K. Molecular Dynamics Simulation for Polymers in the Presence of a Heat Bath. *Phys. Rev. A* **1986**, *33*, 3628–3631.

- (102) Swope, W. C.; Andersen, H. C.; Berens, P. H.; Wilson, K. R. A Computer Simulation Method for the Calculation of Equilibrium Constants for the Formation of Physical Clusters of Molecules: Application to Small Water Clusters. *J. Chem. Phys.* 1982, 76, 637–649.
- (103) Nagle, J. F.; Jablin, M. S.; Tristram-Nagle, S.; Akabori, K. What are the True Values of the Bending Modulus of Simple Lipid Bilayers? *Chem. Phys. Lipids* **2015**, *185*, 3–10.
- (104) Kučerka, N.; Tristram-Nagle, S.; Nagle, J. F. Closer Look at Structure of Fully Hydrated Fluid Phase DPPC Bilayers. *Biophys. J.* **2006**, *90*, L83–L85.
- (105) Humphrey, W.; Dalke, A.; Schulten, K. VMD: Visual Molecular Dynamics. *J. Mol. Graph.* **1996**, *14*, 33–38.